NANO LETTERS
Letter
Cite This: Nano Lett. 2020, 20, 868−873
pubs.acs.org/NanoLett

Observation of Magnetic Skyrmion Bubbles in a van der Waals Ferromagnet Fe_3GeTe_2

Bei Ding,[†,∥,⊥] Zefang Li,[†,∥,⊥] Guizhou Xu,[‡,⊥] Hang Li,[†,∥] Zhipeng Hou,[§] Enke Liu,[†] Xuekui Xi,[†] Feng Xu,[‡] Yuan Yao,[†] and Wenhong Wang*[,†]

[†]Beijing National Laboratory for Condensed Matter Physics, Institute of Physics, Chinese Academy of Sciences, Beijing 100190, China
[‡]School of Materials Science and Engineering, Nanjing University of Science and Technology, Nanjing 210094, China
[§]South China Academy of Advanced Optoelectronics, South China Normal University, Guangzhou 510006, China
[∥]University of Chinese Academy of Sciences, Beijing 100049, China

Supporting Information

ABSTRACT: Two-dimensional (2D) van der Waals (vdW) magnetic materials have recently been introduced as a new horizon in materials science, and they enable potential applications for next-generation spintronic devices. Here, in this communication, the observations of stable Bloch-type magnetic skyrmions in single crystals of 2D vdW Fe_3GeTe_2 (FGT) are reported by using *in situ* Lorentz transmission electron microscopy (TEM). We find the ground-state magnetic stripe domains in FGT transform into skyrmion bubbles when an external magnetic field is applied perpendicularly to the (001) thin plate with temperatures below the Curie temperature T_C. Most interestingly, a hexagonal lattice of skyrmion bubbles is obtained via field-cooling manipulation with magnetic field applied along the [001] direction. Owing to their topological stability, the skyrmion bubble lattices are stable to large field-cooling tilted angles and further reproduced by utilizing the micromagnetic simulations. These observations directly demonstrate that the 2D vdW FGT possesses a rich variety of topological spin textures, being of great promise for future applications in the field of spintronics.

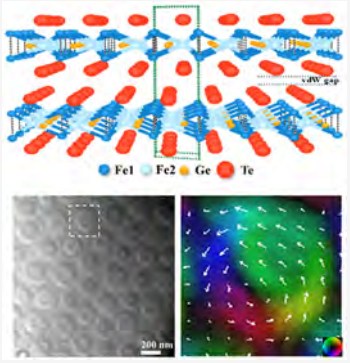

KEYWORDS: *Magnetic skyrmions, van der Waals materials, Fe_3GeTe_2, Lorentz transmission electron microscopy*

Two-dimensional (2D) van der Waals (vdW) materials are a family of quantum materials that have attracted great research attention in the past decade, as they possess a diverse range of novel phenomena which are promising for technological applications.[1,2] In particular, the recent discovery of magnetic 2D vdW materials, such as $Cr_2Si_2Te_6$/$Cr_2Ge_2Te_6$,[3−5] CrI_3/$CrBr_3$,[6,7] and Fe_3GeTe_2 (FGT),[8,9] not only offers exciting opportunities for exploring new physical properties but also opens up a new way for developing spintronic devices by applying magnetism as a possible altering parameter.[10] Among these materials, FGT is the only ferromagnetic metal, in which a long-range ferromagnetic order has been confirmed experimentally ranging from bulk crystals down to monolayers.[11−13] Remarkably, bulk crystalline FGT has the highest Curie temperature T_C (~230 K) and the T_C of layered FGT can be raised to room temperature via electrostatic gating[8,14] or in patterned microstructures.[13] Following this discovery, many intriguing magnetic and transport properties, such as the extremely large anomalous Hall effect,[15] Planar topological Hall effect,[16] Kondo lattice physics,[17] anisotropy magnetostriction effect,[18] and spin filtered tunneling effect,[19] have been observed experimentally in exfoliated FGT nanoflakes and its heterostructures.

Moreover, 2D vdW FGT exhibits a strong out-of-plane uniaxial magnetic anisotropy down to atomic-layer thicknesses,[8,9,14,20] which is very critical for spintronic applications, typically, magnetic-tunneling junctions and magnetic random-access-memory devices. On the other hand, in a magnetic material, the competition between the uniaxial magnetic anisotropy and magnetic dipole−dipole interaction can emerge and lead to a diversity of topological spin configurations that are defined with their unique topological number.[21] For example, magnetic skyrmionic bubbles with various topological spin textures have been experimentally discovered in a range of centrosymmetric magnets, such as perovskite manganites,[21,22] hexagonal MnNiGa alloys,[23−25] and layered kagome Fe_3Sn_2 magnets.[26,27] More importantly, recent theoretical and experimental works have discussed the emergence of topological spin textures including magnetic skyrmions in 2D vdW materials and their heterostructures for future spintronic applications.[28,29] These findings inspire us to investigate the magnetic domain structures and magnetization dynamics of 2D

Received: August 22, 2019
Revised: December 18, 2019
Published: December 23, 2019

DOI: 10.1021/acs.nanolett.9b03453
Nano Lett. 2020, 20, 868−873

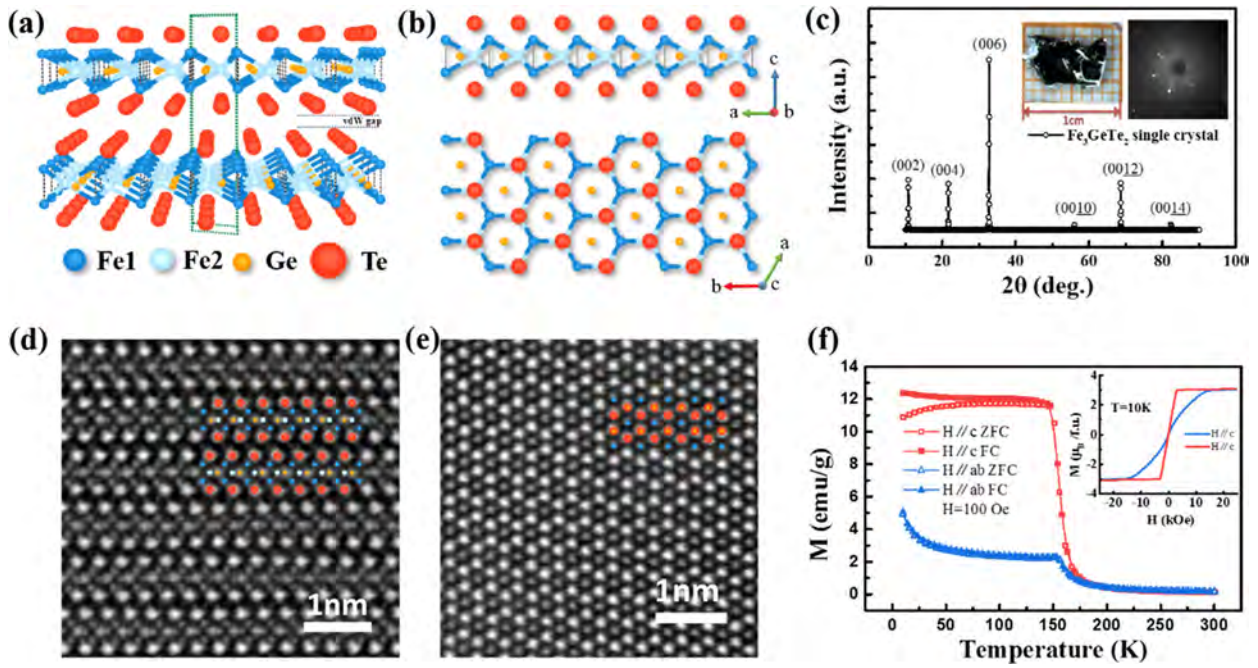

Figure 1. Structure and magnetic properties of a van der Waals (vdW) Fe_3GeTe_2 (FGT) single crystal. (a) Schematic of the structure of a FGT bilayer with an interlayer vdW gap. (b) The crystal structures of monolayered FGT viewed from the *ac* and *ab* planes, respectively. (c) XRD pattern for the as-grown slice of the Fe_3GeTe_2 single crystal. The optical photograph and Laue image in the inset show the typical size and Laue diffraction pattern, indicating the [001] orientation of the single crystal. (d, e) High-resolution STEM HAADF images along the [010] and [001] directions, respectively. The insets show the arrangement of the stacking structure of Te atoms and the hexagonal ring of the Fe_{II}−Ge layer. The scale bar is 1 nm. (f) Temperature dependence of the ZFC and FC magnetization measured at H = 100 Oe for $H//ab$ and $H//c$. The inset shows the anisotropic M−H curve at T = 10 K.

vdW FGT crystals using Lorentz transmission electron microscopy (TEM).

Here, in this work, we report on a Bloch-type magnetic skyrmion bubble which can indeed be observed in the single crystal sample of 2D vdW FGT. Owing to the competition between uniaxial magnetic anisotropy and magnetic dipole−dipole interactions, at temperatures below T_C, we found that the magnetic stripe domains in FGT thin plates turn into magnetic skyrmion bubbles with magnetic field applied perpendicularly to the (001) plane. Moreover, a high-density hexagonally packed lattice of skyrmion bubbles emerges by a simple field-cooling process and keeps stable after reducing the magnetic field to zero. Owing to their topological stability, the skyrmion bubble lattices are stable to large field-cooling tilted angles and further reproduced by utilizing the micromagnetic simulations. These observations directly demonstrate that the 2D vdW FGT possesses a rich variety of topological spin textures, being a great candidate for future applications in the field of spintronics.

Single crystal Fe_3GeTe_2 was synthesized by using the self-flux technique with a mixture of pure elements Ge (99.9999%), Fe (99.99%), and Te (99.995%) (see the Methods Summary in the Supporting Information for details). As schematically shown in Figure 1a,b, the 2D vdW FGT belongs to space group $P63/mmc$ with two Te layers separated by layered Fe_3Ge heterometallic slabs. There are two inequivalent Fe(1) and Fe(2) atoms in the Fe_3Ge slabs, forming two separated triangular lattice Fe(1)−Fe(1) layers and a Fe(2)−Ge hexagonal atomic ring layer.[11] Figure 1c shows the typical X-ray diffraction (XRD) pattern of a bulk FGT single crystal which agrees with the recent work.[30] One can notice that the XRD pattern represents only the (0 0 2n) Bragg peaks (n = 1, 2, 3, 4, 5, 6), indicating that the studied surface is the *ab* plane of the FGT crystal. The crystal structure of FGT crystals was further examined by atomic resolution scanning transmission electron microscopy (STEM), as shown in Figure 1d,e. The bilayer Te atoms are clearly observed in the STEM HAADF image along the [100] axis, as shown in Figure 1d, confirming the layered structure and high quality of our samples. In [001] projection imaging (Figure 1e), we clearly see the arrangement of the hexagonal ring of the Fe(2)−Ge layer and the triangular structure of Fe(1) atoms. The thickness and composition of the FGT thin plate were determined by electron energy loss spectrum (EELS) and scanning energy dispersive X-ray (EDX) spectroscopy, demonstrating the uniform element distribution of Ge, Fe, and Te across the surface (see Figures S1 and S2, Supporting Information).

In Figure 1f, the zero-field-cooling (ZFC) and field-cooling (FC) $M(T)$ curves are measured with external field H = 100 Oe applied both parallel to the *c* direction and in the *ab* plane. Clearly, a paramagnetic to ferromagnetic transition was observed at approximately $T_C \sim 150$ K with both directions, consistent with what was previously reported for the flux-grown samples.[31,32] The magnetization of the two directions ($H//ab$ and $H//c$) exhibits a distinctive difference which is caused by the magnetic anisotropic character of FGT crystals. Moreover, when $H//c$, the FC and ZFC plots have a bifurcation below T_C similar to other typical frustrated magnets.[26,27,33] The inset of Figure 1f shows the magnetization curves measured at T = 10 K with $H//ab$ and $H//c$, respectively. It can be seen that the magnetic easy axis is along $H//c$, revealing a strong magnetic anisotropy in FGT. The saturated magnetic moment (M_S) is 3.25 μ_B/f.u. consistent with the reported values.[11,31,32]

DOI: 10.1021/acs.nanolett.9b03453
Nano Lett. 2020, 20, 868−873

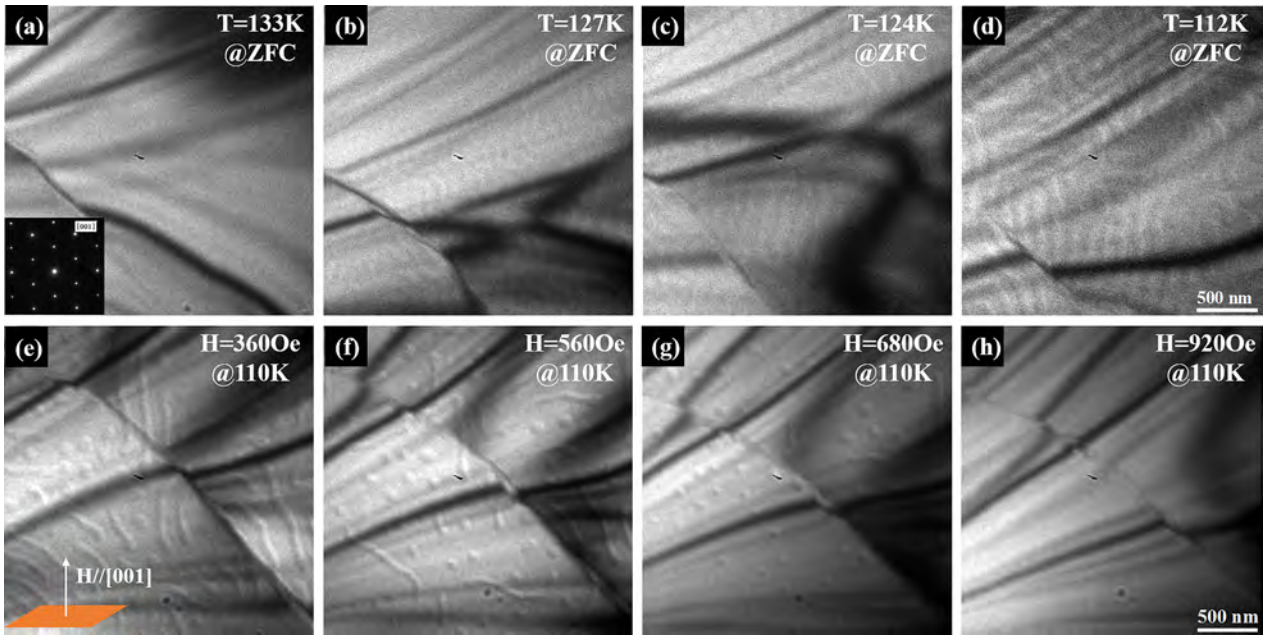

Figure 2. Representative images of the domain structures of a vdW FGT thin plate taken by Lorentz-TEM with an electron beam perpendicular to the *ab* plane. (a–d) The underfocused Lorentz-TEM images of FGT when the sample temperature was lowered from 300 to 100 K in a zero-field-cooling (ZFC) process. The inset of part (a) shows the corresponding selected-area electron diffraction (SAED) pattern. At temperatures below 130 K, a spontaneous ground state of the stripe domain appears and becomes more clear at a lower temperature of 112 K shown in Figure 2d. (e–h) The underfocused Lorentz-TEM images showing magnetic-field-driven transitions from stripes (d) gradually to bubbles (e–g) and eventually ferromagnetic state (h) with different external magnetic fields (H) applied along the *c*-axis at T = 110 K. The scale bar is 500 nm.

Figure 2a–d shows the evolution of magnetic domain structures as a function of temperature observed by using *in situ* Lorentz-TEM under zero magnetic field (see Supplementary Movie 1, Supporting Information). The corresponding view area is along the [001] direction, which is presented though selected-area electron diffraction (SAED) measurements (see the inset of Figure 2a). We noticed that, at temperatures below $T_C \sim 150$ K, the magnetic stripe domains emerge with an average width of ~120 nm, as shown in Figure 2b. This value is comparable to that in the MnNiGa[23] and Fe_3Sn_2[26] while roughly 2 times larger than that in the $La_{1-x}Sr_xMnO_3$ (x = 0.175).[22] The characteristic bright and dark magnetic contrast appears in the sample, indicating that the spin of the magnetic stripe domains stands upward and downward along the magnetic easy axis which are separated by Bloch domain walls. As the temperature decreased, the magnetic stripes became wider and more distinct, while the domain wall still remained in the original state. One should note that the critical temperatures T_C of the Lorentz-TEM sample are consistent with those of the bulk samples.

To confirm the variation of magnetic stripe domains under an application of magnetic field, we then investigated the magnetic domain texture evolution under different magnetic fields at T = 110 K, shown in Figure 2e–h. The magnetic field was applied along the [001] direction by increasing the objective lens current. The corresponding dynamics of formation and disappearance of the skyrmion bubbles with increasing applied magnetic field were successfully recorded by using *in situ* Lorentz-TEM (see Figure S3, Supporting Information). Remarkably, the magnetic stripe domain structure gradually transformed into skyrmion bubbles is spotted with the magnetic field increasing from 0 to 920 Oe. At a lower magnetic field, the magnetic stripe domain parallels to the external field expanding at the expense of the antiparallel ones. Figure 2e displays an image of the transformation procedure under a magnetic field of 360 Oe. It is clear that the stripe domains, fragmentary magnetic domains together with skyrmion bubbles, exist in this state. With the increase of magnetic field (Figure 2f–h), the evolution from residual magnetic stripe domains to the dumbbell-shaped magnetic domains first gradually occurs before totally shrinking into the skyrmion bubbles. As the magnetic field increases further above 680 Oe, the dumbbell-shaped magnetic stripes are completely replaced by skyrmion bubbles. With further increasing magnetic field, the size of the skyrmion bubbles decreases and eventually disappears in the ferromagnetic state (Figure 2h) (see Figure S4 for the detailed analysis, Supporting Information). These observations clearly indicate that an isolated skyrmion bubble can be obtained in the 2D vdW FGT magnet by applying the magnetic field perpendicular to the thin plate. The saturated magnetic field of the Lorentz-TEM sample coincides with that of the bulk sample measured by magnetization (see Figure S5, Supporting Information), which can arise from the fact that the magnetic anisotropy in FGT is high enough to overcome the increase of demagnetizing energy in the thin Lorentz-TEM sample. At T = 10 K, the uniaxial magnetic anisotropy constant K_u of FGT single crystals is calculated to be as large as $\approx 10^7$ erg cm^{-3}, consistent with the reported values.[10]

Figure 3a–d shows the detailed evolution of magnetic domain structures as a function of temperature at a fixed magnetic field of 600 Oe; the specific field-cooling (FC) manipulation is the same as our previous work.[34] Although the Lorentz-TEM image appears to have some scratches due to the iron milling which further results in a slight distorting of the magnetization distribution, it will not affect the observation of the bubble lattices. The magnetic domain appears contrasted at ~124 K (Figure 3b) and gradually forms a single skyrmion

DOI: 10.1021/acs.nanolett.9b03453
Nano Lett. 2020, 20, 868–873

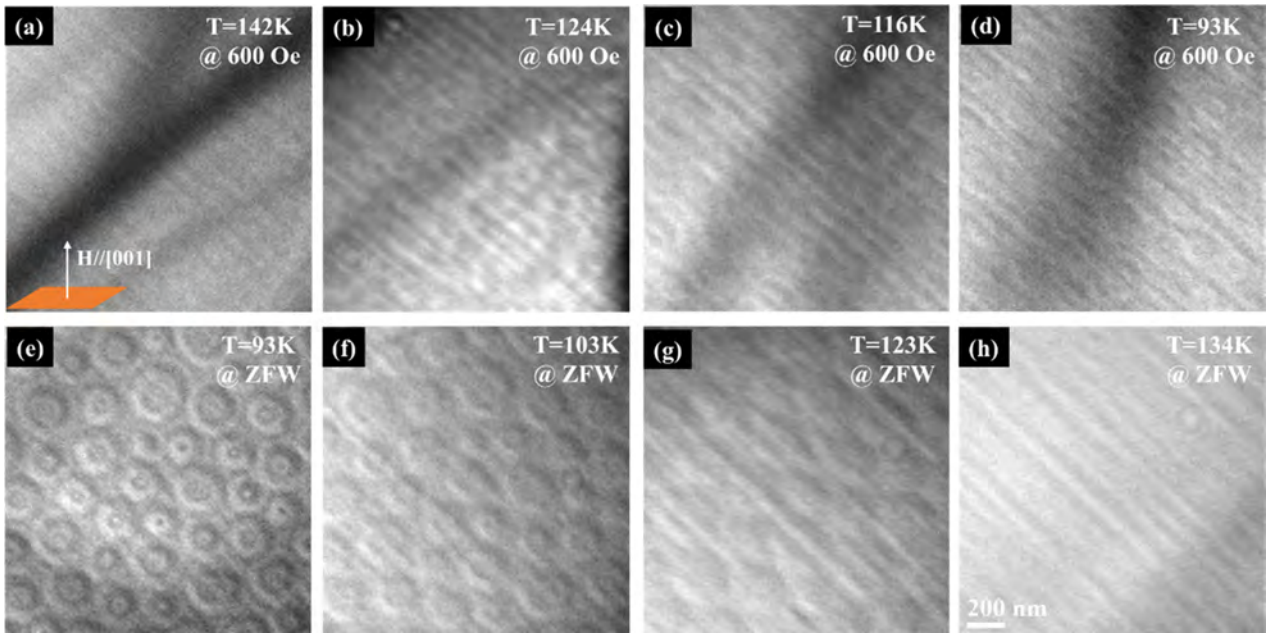

Figure 3. (a–d) The underfocused Lorentz-TEM images of FGT when the sample temperature was lowered from 300 to 93 K in a 600 Oe field-cooling (FC) process. The high-density skyrmion lattices are confirmed at temperatures below $T_C \sim 150$ K after the FC procedure. (e–h) The underfocused Lorentz-TEM images showing the bubble lattice evolution during a zero-field-warming (ZFW) process. The scale bar is 200 nm.

bubble at a temperature of about 116 K (Figure 3c). When we decrease the temperature to 93 K (below $T_C \sim 150$ K) during the FC process, a hexagonal lattice of skyrmion bubbles is obtained, as shown in Figure 3d. Most interestingly, the bubble lattices remain unchanged after turning off the field to zero (Figure 3e). The zero-field stabilized lattice of skyrmion bubbles is probably a metastable state, during the zero-field-warming (ZFW) process, as shown in Figure 3e–g, causing a little bit of size decrease and then gradually changing into the stripe domains (see Supplementary Movie 2, Supporting Information). As T_C is approached, the magnetic contrast becomes weaker at ~134 K (Figure 3h) due to the decreased amplitude of the magnetization and increased thermal disorder. These results are similar to the skyrmion bubble lattices reported in other centrosymmetric magnets, such as tetragonal perovskite magnetites[22] and hexagonal MnNiGa alloys.[24] Thus, it turns out that the magnetic fields play a critical role during the FC process to generate the highest-density hexagonal lattice of skyrmion bubbles. On the other hand, we should point out that, after the FC manipulation, the zero-field stabilized bubble lattices are found for the entire temperature range down to 93 K. This result is similar to that of MnNiGa alloy[24] but intrinsically different from that of chiral magnets, where the skyrmion phase exists only in the narrow area below T_C.[35−37]

In the centrosymmetric magnets, the competition between the perpendicular magnetic anisotropy and magnetic dipole–dipole interaction is the crucial point in the generation of skyrmion bubbles. As a result, the spin textures of skyrmion bubbles in these materials are highly sensitive to the direction of the applied magnetic field related to the easy axis.[38] To examine the stability of the skyrmion bubbles observed in the FGT magnet in detail, we have further preformed the FC Lorentz-TEM experiments with a fixed magnetic field of 600 Oe applied at various oblique angles; i.e., the FGT sample was tilted with $\alpha = \pm 20°$ along the x-axis and $\beta = -10°$ along the y-axis, respectively. Figure 4a–d shows the magnetic configuration observed at zero-field after various FC manipulations mentioned above. Remarkably, the FC procedure at different tilted angles can generate skyrmion bubbles and arrange them into a hexagonal lattice. These results agree well with a theoretical simulation of the bubble lattice generation in a small oblique field, as shown in Figure S6, Supporting Information.

In order to better clarify the spin configuration of the skyrmion bubbles observed in the FGT magnet, in Figure 4e and f, we show the under- and overfocused Lorentz-TEM images of the zero-field stabilized lattice of skyrmion bubbles, respectively. The sharp contrast variations from dark to bright ring in the underfocused image identified with the Bloch domain walls separate the spin-up and spin-down domains. It represents a reversal image contrast in the overfocused image shown in Figure 4f. The in-plane magnetization distribution map based on transport of intensity equation (TIE) analysis for a selected skyrmion bubble is shown in Figure 4g (see Figure S7 for the TIE analysis of the skyrmion bubble lattice), where white arrows indicate the size and direction of the magnetic component at each point. Clearly, the topological spin texture of a skyrmion bubble rotated counterclockwise, forming a vortex-like magnetic domain, which is consistent with the Bloch-type skyrmion observed in both non-centrosymmetric (such as FeGe[39] and MnSi[40]) and centrosymmetric (such as Fe_3Sn_2[26] and Ba–Fe–Sc–Mn–O[21]) magnets. These experimental results agree well with our theoretical simulations of the skyrmion bubbles in FGT magnets, as shown in Figure 4h, where the enclosed circular shape magnetic structures are revealed, signifying the presence of Bloch-type skyrmions.

In conclusion, we have demonstrated the formation of Bolch-type skyrmions in the 2D vdW FGT crystals. Owing to their topological stability, the densely hexagonal lattices of skyrmion bubbles are stable to large tilted angles at zero-field after subjecting a field-cooling manipulation. The stable skyrmion bubble lattices that we observed are important for

DOI: 10.1021/acs.nanolett.9b03453
Nano Lett. 2020, 20, 868–873

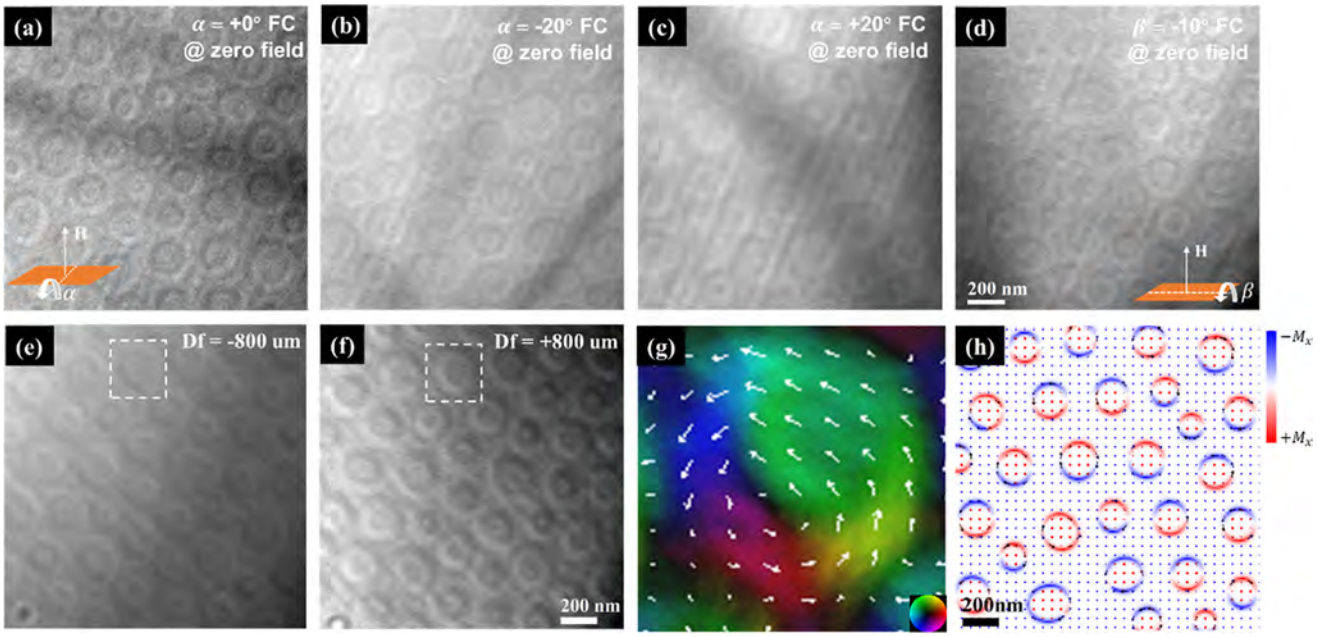

Figure 4. (a–d) Underfocused Lorentz-TEM image of skyrmion bubbles at 93 K after FC manipulation with a field (600 Oe) applied with rotation angles. (α; as shown schematically in the inset of (a) $\alpha = -20°$, (b) $\alpha = 0°$, (c) $\alpha = +20°$, and (d) $\beta = -10°$, respectively). (e, f) Underfocused and overfocused Lorentz-TEM images of the skyrmion bubbles taken at 93 K and in zero-field. (g) An enlarged in-plane magnetization distribution map obtained by TIE analysis for a selected skyrmion bubble indicated by the white dotted box in parts e and f. The white arrows represent the magnetization direction at each point, and the color wheel is in the right corner. (h) Theoretical simulation of skyrmion lattices at an applied magnetic field with 600 Oe for $\alpha = 0°$. The in-plane magnetization distribution is represented by blue ($-M_x$) and red ($+M_x$) regions. The scale bar is 200 nm.

the exploitation of 2D vdW skyrmion-based devices and are likely to have a strong effect on magnetic and magnetotransport properties in these 2D vdW crystals. It should be pointed out that, during the submission of this manuscript, the Bloch-type skyrmion bubbles are also observed in another 2D vdW magnet $Cr_2Ge_2Te_6$.[41] Moreover, observations of the Neel-type skyrmions in a thinner FGT film and its heterostructure have recently been reported on the arXiv by T.-E. Park et al., Y. Wu et al., and H. Wang et al.,[42−44] respectively. Additionally, transformation from stripy domains into multi-circular bubble domains as well as the Neel-type chiral domain wall have been observed in cleaved FGT by scanning tunneling microscope.[45] We thus anticipate that the tunable nature of 2D vdW magnets will enable the formation of a wide range of topological spin textures, by varying the thickness, the spin−orbit coupling, the interfacial symmetry of heterostructures, and thereby the magnetocrysalline anisotropy and the magnetization.

■ ASSOCIATED CONTENT

Supporting Information

The Supporting Information is available free of charge at https://pubs.acs.org/doi/10.1021/acs.nanolett.9b03453.

Additional experimental details including single crystal growth, structure and magnetic measurement, Curie temperature determination, magnetic-stripe domains and formation of magnetic skyrmion bubbles, and micromagnetic simulation results in single crystals of Fe_3GeTe_2 (PDF)

Supplementary Movie 1 showing the evolution of magnetic domain structures as a function of temperature observed by using *in situ* Lorentz-TEM under a zero magnetic field (MP4)

Supplementary Movie 2 showing the zero-field-warming (ZFW) process of skyrmion bubbles recorded by using *in situ* Lorentz-TEM under a zero magnetic field (MP4)

■ AUTHOR INFORMATION

Corresponding Author

*E-mail: wenhong.wang@iphy.ac.cn.

ORCID

Wenhong Wang: 0000-0002-0641-3792

Author Contributions

⊥B.D., Z.L., and G.X. contributed equally to this work.

Notes

The authors declare no competing financial interest.

■ ACKNOWLEDGMENTS

This work is supported by the National Key R&D Program of China (2017YFA0303202 and 2017YFA0206303), the National Natural Science Foundation of China (11604148 and 11874410), and Beijing Natural Science Foundation (Grant No. Z190009)

■ REFERENCES

(1) Geim, A. K.; Grigorieva, I. V. *Nature* **2013**, *499*, 419.

(2) Novoselov, K. S.; Mishchenko, A.; Carvalho, A.; Castro Neto, A. H. *Science* **2016**, *353* (6298), aac9439.

(3) Carteaux, V.; Brunet, D.; Ouvrard, G.; Andre, G. *J. Phys.: Condens. Matter* **1995**, *7* (1), 69−87.

(4) Siberchicot, B.; Jobic, S.; Carteaux, V.; Gressier, P.; Ouvrard, G. *J. Phys. Chem.* **1996**, *100* (14), 5863−5867.

(5) Gong, C.; Li, L.; Li, Z.; Ji, H.; Stern, A.; Xia, Y.; Cao, T.; Bao, W.; Wang, C.; Wang, Y.; Qiu, Z. Q.; Cava, R. J.; Louie, S. G.; Xia, J.; Zhang, X. *Nature* **2017**, *546*, 265.

DOI: 10.1021/acs.nanolett.9b03453
Nano Lett. 2020, 20, 868−873

(6) Jiang, S.; Li, L.; Wang, Z.; Mak, K. F.; Shan, J. *Nat. Nanotechnol.* **2018**, *13* (7), 549−553.
(7) Huang, B.; Clark, G.; Navarro-Moratalla, E.; Klein, D. R.; Cheng, R.; Seyler, K. L.; Zhong, D.; Schmidgall, E.; McGuire, M. A.; Cobden, D. H.; Yao, W.; Xiao, D.; Jarillo-Herrero, P.; Xu, X. *Nature* **2017**, *546*, 270.
(8) Deng, Y.; Yu, Y.; Song, Y.; Zhang, J.; Wang, N. Z.; Sun, Z.; Yi, Y.; Wu, Y. Z.; Wu, S.; Zhu, J.; Wang, J.; Chen, X. H.; Zhang, Y. *Nature* **2018**, *563* (7729), 94−99.
(9) Fei, Z.; Huang, B.; Malinowski, P.; Wang, W.; Song, T.; Sanchez, J.; Yao, W.; Xiao, D.; Zhu, X.; May, A. F.; Wu, W.; Cobden, D. H.; Chu, J.-H.; Xu, X. *Nat. Mater.* **2018**, *17* (9), 778−782.
(10) Li, H.; Ruan, S.; Zeng, Y.-J. *Adv. Mater.* **2019**, *31* (27), 1900065.
(11) Deiseroth, H.-J.; Aleksandrov, K.; Reiner, C.; Kienle, L.; Kremer, R. K. *Eur. J. Inorg. Chem.* **2006**, *2006* (8), 1561−1567.
(12) Chen, B.; Yang, J.; Wang, H.; Imai, M.; Ohta, H.; Michioka, C.; Yoshimura, K.; Fang, M. *J. Phys. Soc. Jpn.* **2013**, *82* (12), 124711.
(13) Li, Q.; Yang, M.; Gong, C.; Chopdekar, R. V.; N'Diaye, A. T.; Turner, J.; Chen, G.; Scholl, A.; Shafer, P.; Arenholz, E.; Schmid, A. K.; Wang, S.; Liu, K.; Gao, N.; Admasu, A. S.; Cheong, S.-W.; Hwang, C.; Li, J.; Wang, F.; Zhang, X.; Qiu, Z. *Nano Lett.* **2018**, *18* (9), 5974−5980.
(14) Klein, D. R.; MacNeill, D.; Lado, J. L.; Soriano, D.; Navarro-Moratalla, E.; Watanabe, K.; Taniguchi, T.; Manni, S.; Canfield, P.; Fernández-Rossier, J.; Jarillo-Herrero, P. *Science* **2018**, *360* (6394), 1218−1222.
(15) Kim, K.; Seo, J.; Lee, E.; Ko, K. T.; Kim, B. S.; Jang, B. G.; Ok, J. M.; Lee, J.; Jo, Y. J.; Kang, W.; Shim, J. H.; Kim, C.; Yeom, H. W.; Il Min, B.; Yang, B.-J.; Kim, J. S. *Nat. Mater.* **2018**, *17* (9), 794−799.
(16) You, Y.; Gong, Y.; Li, H.; Li, Z.; Zhu, M.; Tang, J.; Liu, E.; Yao, Y.; Xu, G.; Xu, F.; Wang, W. *Phys. Rev. B: Condens. Matter Mater. Phys.* **2019**, *100* (13), 134441.
(17) Zhang, Y.; Lu, H.; Zhu, X.; Tan, S.; Feng, W.; Liu, Q.; Zhang, W.; Chen, Q.; Liu, Y.; Luo, X.; Xie, D.; Luo, L.; Zhang, Z.; Lai, X. *Sci. Adv.* **2018**, *4* (1), No. eaao6791.
(18) Zhuang, H. L.; Kent, P. R. C.; Hennig, R. G. *Phys. Rev. B: Condens. Matter Mater. Phys.* **2016**, *93* (13), 134407.
(19) Song, T.; Cai, X.; Tu, M. W.-Y.; Zhang, X.; Huang, B.; Wilson, N. P.; Seyler, K. L.; Zhu, L.; Taniguchi, T.; Watanabe, K.; McGuire, M. A.; Cobden, D. H.; Xiao, D.; Yao, W.; Xu, X. *Science* **2018**, *360* (6394), 1214−1218.
(20) Verchenko, V. Y.; Tsirlin, A. A.; Sobolev, A. V.; Presniakov, I. A.; Shevelkov, A. V. *Inorg. Chem.* **2015**, *54* (17), 8598−8607.
(21) Yu, X.; Mostovoy, M.; Tokunaga, Y.; Zhang, W.; Kimoto, K.; Matsui, Y.; Kaneko, Y.; Nagaosa, N.; Tokura, Y. *Proc. Natl. Acad. Sci. U. S. A.* **2012**, *109* (23), 8856−8860.
(22) Yu, X.; Morikawa, D.; Tokunaga, Y.; Kubota, M.; Kurumaji, T.; Oike, H.; Nakamura, M.; Kagawa, F.; Taguchi, Y.; Arima, T.-h.; Kawasaki, M.; Tokura, Y. *Adv. Mater.* **2017**, *29* (21), 1606178.
(23) Wang, W.; Zhang, Y.; Xu, G.; Peng, L.; Ding, B.; Wang, Y.; Hou, Z.; Zhang, X.; Li, X.; Liu, E.; Wang, S.; Cai, J.; Wang, F.; Li, J.; Hu, F.; Wu, G.; Shen, B.; Zhang, X.-X. *Adv. Mater.* **2016**, *28* (32), 6887−6893.
(24) Peng, L.; Zhang, Y.; Wang, W.; He, M.; Li, L.; Ding, B.; Li, J.; Sun, Y.; Zhang, X. G.; Cai, J.; Wang, S.; Wu, G.; Shen, B. *Nano Lett.* **2017**, *17* (11), 7075−7079.
(25) Li, X.; Zhang, S.; Li, H.; Venero, D. A.; White, J. S.; Cubitt, R.; Huang, Q.; Chen, J.; He, L.; van der Laan, G.; Wang, W.; Hesjedal, T.; Wang, F. *Adv. Mater.* **2019**, *31* (17), 1900264.
(26) Hou, Z.; Ren, W.; Ding, B.; Xu, G.; Wang, Y.; Yang, B.; Zhang, Q.; Zhang, Y.; Liu, E.; Xu, F.; Wang, W.; Wu, G.; Zhang, X.; Shen, B.; Zhang, Z. *Adv. Mater.* **2017**, *29* (29), 1701144.
(27) Hou, Z.; Zhang, Q.; Xu, G.; Gong, C.; Ding, B.; Wang, Y.; Li, H.; Liu, E.; Xu, F.; Zhang, H.; Yao, Y.; Wu, G.; Zhang, X.-x.; Wang, W. *Nano Lett.* **2018**, *18* (2), 1274−1279.
(28) Tong, Q.; Liu, F.; Xiao, J.; Yao, W. *Nano Lett.* **2018**, *18* (11), 7194−7199.
(29) Behera, A. K.; Chowdhury, S.; Das, S. R. *Appl. Phys. Lett.* **2019**, *114* (23), 232402.
(30) Alghamdi, M.; Lohmann, M.; Li, J.; Jothi, P. R.; Shao, Q.; Aldosary, M.; Su, T.; Fokwa, B. P. T.; Shi, J. *Nano Lett.* **2019**, *19* (7), 4400−4405.
(31) May, A. F.; Calder, S.; Cantoni, C.; Cao, H.; McGuire, M. A. *Phys. Rev. B: Condens. Matter Mater. Phys.* **2016**, *93* (1), 014411.
(32) Liu, Y.; Ivanovski, V. N.; Petrovic, C. *Phys. Rev. B: Condens. Matter Mater. Phys.* **2017**, *96* (14), 144429.
(33) Hou, Z.; Zhang, Q.; Xu, G.; Zhang, S.; Gong, C.; Ding, B.; Li, H.; Xu, F.; Yao, Y.; Liu, E.; Wu, G.; Zhang, X.-x.; Wang, W. *ACS Nano* **2019**, *13* (1), 922−929.
(34) Ding, B.; Cui, J.; Xu, G.; Hou, Z.; Li, H.; Liu, E.; Wu, G.; Yao, Y.; Wang, W. *Phys. Rev. Appl.* **2019**, *12* (5), 054060.
(35) Mühlbauer, S.; Binz, B.; Jonietz, F.; Pfleiderer, C.; Rosch, A.; Neubauer, A.; Georgii, R.; Böni, P. *Science* **2009**, *323* (5916), 915−919.
(36) Neubauer, A.; Pfleiderer, C.; Binz, B.; Rosch, A.; Ritz, R.; Niklowitz, P. G.; Böni, P. *Phys. Rev. Lett.* **2009**, *102* (18), 186602.
(37) Kanazawa, N.; Seki, S.; Tokura, Y. *Adv. Mater.* **2017**, *29* (25), 1603227.
(38) Ding, B.; Li, H.; Li, X.; Wang, Y.; Hou, Z.; Xu, G.; Liu, E.; Wu, G.; Wang, F.; Wang, W. *APL Mater.* **2018**, *6* (7), 076101.
(39) Yu, X. Z.; Kanazawa, N.; Onose, Y.; Kimoto, K.; Zhang, W. Z.; Ishiwata, S.; Matsui, Y.; Tokura, Y. *Nat. Mater.* **2011**, *10* (2), 106−9.
(40) Tonomura, A.; Yu, X.; Yanagisawa, K.; Matsuda, T.; Onose, Y.; Kanazawa, N.; Park, H. S.; Tokura, Y. *Nano Lett.* **2012**, *12* (3), 1673−1677.
(41) Han, M. G.; Garlow, J. A.; Liu, Y.; Zhang, H.; Li, J.; DiMarzio, D.; Knight, M. W.; Petrovic, C.; Jariwala, D.; Zhu, Y. *Nano Lett.* **2019**, *19* (11), 7859−7865.
(42) Park, T.-E.; Peng, L.; Liang, J.; Hallal, A.; Zhang, X.; Jong Kim, S.; Song, K. M.; Kim, K.; Weigand, M.; Schuetz, G.; Finizio, S.; Raabe, J.; Xia, J.; Zhou, Y.; Ezawa, M.; Liu, X.; Chang, J.; Koo, H. C.; Duck Kim, Y.; Chshiev, M.; Fert, A.; Yang, H.; Yu, X.; Woo, S. *arXiv:1907.01425* (2019).
(43) Wu, Y.; Zhang, S.; Zhang, J.; Wang, W.; Zhu, Y. L.; Hu, J.; Wong, K.; Fang, C.; Wan, C.; Han, X.; Shao, Q.; Taniguchi, T.; Watanabe, K.; Mao, Z.; Zhang, X.; Wang, K. L. *arXiv:1907.11349* (2019).
(44) Wang, H.; Wang, C.; Zhu, Y.; Li, Z.-A.; Zhang, H.; Tian, H.; Shi, Y.; Yang, H.; Li, J. *arXiv:1907.08382* (2019).
(45) Nguyen, G. D.; Lee, J.; Berlijn, T.; Zou, Q.; Hus, S. M.; Park, J.; Gai, Z.; Lee, C.; Li, A.-P. *Phys. Rev. B: Condens. Matter Mater. Phys.* **2018**, *97* (1), 014425.

DOI: 10.1021/acs.nanolett.9b03453
Nano Lett. 2020, 20, 868−873